Perfect synchronization in complex networks with higher-order interactions

Sangita Dutta,[1] Prosenjit Kundu,[2,*] Pitambar Khanra,[3] Chittaranjan Hens,[4] and Pinaki Pal[1,†]
[1]*Department of Mathematics, National Institute of Technology, Durgapur 713209, India*
[2]*Dhirubhai Ambani Institute of Information and Communication Technology, Gandhinagar, Gujarat 382007, India*
[3]*Department of Mathematics, University at Buffalo, State University of New York, Buffalo, New York 14260, USA*
[4]*Center for Computational Natural Science and Bioinformatics, International Institute of Informational Technology, Gachibowli, Hyderabad 500032, India*

(Received 15 February 2023; accepted 11 July 2023; published 8 August 2023)

Achieving perfect synchronization in a complex network, specially in the presence of higher-order interactions (HOIs) at a targeted point in the parameter space, is an interesting, yet challenging task. Here we present a theoretical framework to achieve the same under the paradigm of the Sakaguchi-Kuramoto (SK) model. We analytically derive a frequency set to achieve perfect synchrony at some desired point in a complex network of SK oscillators with higher-order interactions. Considering the SK model with HOIs on top of the scale-free, random, and small world networks, we perform extensive numerical simulations to verify the proposed theory. Numerical simulations show that the analytically derived frequency set not only provides stable perfect synchronization in the network at a desired point but also proves to be very effective in achieving a high level of synchronization around it compared to the other choices of frequency sets. The stability and the robustness of the perfect synchronization state of the system are determined using the low-dimensional reduction of the network and by introducing a Gaussian noise around the derived frequency set, respectively.

DOI: 10.1103/PhysRevE.108.024304

I. INTRODUCTION

Higher-order structures, such as three- and four-way interactions in addition to pairwise interactions, are widespread in neurological, biological, ecological, and sociological systems [1–14]. In ecological systems such higher-order interactions (HOIs) where three or more species interact with each other can stabilize large ecological communities [15–17]. On the other hand, recent studies have suggested that the mesoscopic organization of the brain through higher-order interactions allows efficient information processing and offers useful guidelines for performing complex tasks [14,18–20]. Motivated by these practical implications, the network science community is also concentrating on understanding the various types of collective behavior ranging from synchronization to epidemic spreading that can go beyond conventional paired interactions [2,3,21–23].

Synchronization observed in the flocking pattern of birds, or rhythmic flashing of fireflies, can be modeled with the interacting nonlinear dynamical units [24–29]. The classic Kuramoto dynamics, one of the celebrated dynamical models used for studying synchronization [30,31], encodes the phase evolution of each node. In a complex network, nodes with nonidentical natural frequencies are connected to one another via paired linkages. Depending on the coupling configuration or particular frequency design, such complicated pairwise connections could cause the entire system to reveal "continuous," "discontinuous," or "optimal" synchronization [22,30,32–37]. However, a slight phase-lag between the oscillators may destabilize or erode the stable synchronization states and destroy the switchlike discontinuous synchronization transition for certain cases [38–44]. Against this backdrop, we explore the impact of HOIs in a network of coupled phase-lag oscillators. Particularly, in the presence of HOIs and fixed coupling strength, we seek a suitable frequency set which can lead the system to a *perfect* [39] global synchronization state where all phases are in unison.

The HOI can induce abrupt synchronization transitions between the incoherent state and the coherent state without any correlations between network structure and dynamical functions. These synchronized states are stable even in the presence of repulsive pairwise coupling due to such higher-order interaction [45]. In a system, three-way interactions in addition to pairwise interactions can cause abrupt desynchronization transitions without any abrupt synchronization transitions, and extensive multistable partially synchronized states [22] may appear.

In particular, interactions in 2-simplexes are important in describing correlation in neuronal activity in the brain [46], providing a missing link between the structure and the dynamics. In fact, considering HOIs is useful where different types of correlation exist between the nodes in a coupled oscillator system. Despite these findings, enhancement of synchronization in phase-frustrated dynamics with higher-order interaction has not been explored so far.

It has been demonstrated that a trade-off between pairwise and higher-order interactions can result in a higher level of synchronization (optimal synchronization) in

*jitprosen.math@gmail.com
†pinaki.pal@maths.nitdgp.ac.in

relatively weaker coupling strength [47] by using an optimal frequency set obtained from the dominant eigenvector of the composite Laplacian, which encodes both pairwise and triangular interactions in the absence of phase frustration. Although phase frustration or phase lag has been shown to have nontrivial effects on the dynamics of paired networked systems [39,40,42,43,48–50], its impact on networks with higher-order interactions has received the least attention.

In this paper, we focus on the topic of targeted global synchronization in phase-frustrated (-lag) complex networks in the presence of pairwise as well as higher-order interactions and ask the question *"Can we determine a set of frequencies to achieve perfect synchronization at a targeted point of the parameter space in such networks?"* In the process, we employ the analytical approaches reported in Refs. [39,51] and develop a framework based on linear theory to achieve the goal of perfect synchronization at a targeted point. The analytical approach eventually leads to the determination of a set of frequencies involving the structural and dynamical properties of the network for the achievement of perfect synchronization. Detailed numerical demonstration with different networks following the analytic finally confirms the achievement of targeted perfect synchronization using the derived frequency.

The organization of the paper is as follows. Sections II and III describe the model and the analytical frame work for deriving a frequency set for the achievement of perfect synchronization at a targeted point. Section IV presents the detailed numerical results on perfect synchronization in different networks. Then, the stability and robustness of the synchronization states are presented in Secs. V and VI. A general discussion and conclusions are made in Sec. VII. We proceed with the model description in the next section.

II. MODEL DESCRIPTION

We consider different networks of coupled Sakaguchi-Kuramoto (SK) [26,43] phase oscillators of size N with higher-order interactions along with pairwise interactions [22,45,52]. The dynamics of each oscillator in the network is governed by the equation

$$\dot{\theta}_i = \omega_i + K_1 \sum_{j=1}^{N} A_{ij} \sin(\theta_j - \theta_i - \alpha) + \frac{K_2}{2} \sum_{j=1}^{N} \sum_{l=1}^{N} B_{ijl} \sin(2\theta_j - \theta_l - \theta_i - \beta), \quad i = 1, 2, \ldots, N, \tag{1}$$

where θ_i is the phase and ω_i is the intrinsic natural frequency of the ith oscillator. α and β act as the frustration terms in the system, corresponding to the pairwise and the triadic interactions, respectively. K_1 and K_2 are the coupling strengths associated with the 1-simplex (pairwise interaction) and the 2-simplex (triadic interaction), respectively. A_{ij} is the ijth element of the adjacency matrix $A = (A_{ij})_{N\times N}$ associated with the 1-simplex, where $A_{ij} = 1$, if the ith and jth nodes are connected, and $A_{ij} = 0$, otherwise. Similarly, B_{ijl} is the adjacency tensor associated with the 2-simplex, where $B_{ijl} = 1$ if there is a triadic connection between the ith, jth, and lth nodes, and $B_{ijl} = 0$, otherwise. Note that the networks under consideration are undirected. As a result, we have $A_{ij} = A_{ji}$ and $B_{ijl} = B_{ilj} = B_{jil} = B_{lji} = B_{lij} = B_{jli}$ for all admissible i and j. Here we choose the 2-simplicial complex, which leads to the consideration of the triadic and pairwise interactions only. By the definition of a simplicial complex, every link in that triangle will be in the simplicial complex. So, the adjacency tensor can be written in the form $B_{ijl} = A_{ij}A_{jl}A_{li}$.

To quantify the level of synchronization in the network, we use the Kuramoto order parameter r given by

$$re^{i\psi(t)} = \frac{1}{N} \sum_{j=1}^{N} e^{i\theta_j}, \tag{2}$$

where $\psi(t)$ is the average phase of the oscillators at time t. The value of the order parameter lies between 0 and 1. $r = 0$ indicates the system is in the incoherent state, while $r = 1$ indicates the fully synchronized state of the system. The coupled equation (1) is used to develop an analytical framework for the achievement of perfect synchronization in the network. The details are described in the next section.

III. ANALYTICAL FRAMEWORK

Here we describe the analytical framework used to derive a frequency set for achieving perfect synchronization at a targeted point in the parameter space following the approach reported in Refs. [39,51]. Linearization of the system (1) about the synchronized state ($|\theta_j - \theta_i| \to 0$) leads to the equation

$$\dot{\theta}_i = \omega_i + \left[-K_1 k_i^{(1)} \sin\alpha - K_2 k_i^{(2)} \sin\beta \right] - K_1 \cos\alpha \left[k_i^{(1)}\theta_i - \sum_{j=1}^{N} A_{ij}\theta_j \right] - K_2 \cos\beta \left[k_i^{(2)}\theta_i - \sum_{j=1}^{N} A_{ij} \left(\sum_{l=1}^{N} A_{jl}A_{li} \right) \theta_j + \frac{1}{2} \sum_{j=1}^{N} A_{ji} \left(\sum_{l=1}^{N} A_{il}A_{lj} \right) \theta_j \right] \quad (i = 1, 2, \ldots, N). \tag{3}$$

The above equation can be written in vector form as

$$\dot{\boldsymbol{\theta}} = \boldsymbol{\omega} + \boldsymbol{d} - L\boldsymbol{\theta}, \tag{4}$$

where $d = -K_1\boldsymbol{k^{(1)}} \sin\alpha - K_2\boldsymbol{k^{(2)}} \sin\beta$ and $L = K_1 \cos\alpha L^{(1)} + K_2 \cos\beta L^{(2)}$ is the composite Laplacian consisting of the Laplacian of pairwise interaction and the Laplacian of triadic interaction, $L^{(1)}$ and $L^{(2)}$, respectively. Here, $L^{(1)}$ and $L^{(2)}$ are defined as

$$L^{(1)} = D^{(1)} - A^{(1)} \quad \text{and} \quad L^{(2)} = D^{(2)} - \left(A^{(2)} - \frac{A^{(2)T}}{2} \right),$$

where $A^{(1)}$ denotes the adjacency matrix A, $D^{(1)} = \text{diag}(k_1^{(1)}, k_2^{(1)}, \ldots, k_N^{(1)})$, $A^{(2)} = A * (A^2)^T$, and $D^{(2)} = \text{diag}(k_1^{(2)}, k_2^{(2)}, \ldots, k_N^{(2)})$, with $*$ denoting the Hadamard product. Also, $k_i^{(1)} = \sum_{j=1}^{N} A_{ij}$ is the degree of the ith node considering the pairwise interaction only and $k_i^{(2)} = \frac{1}{2}\sum_{j=1}^{N}\sum_{l=1}^{N} B_{ijl}$ is the degree of the ith node while considering the triadic interactions.

Now, we derive the steady-state solution by suitably varying the reference frame as $\omega \to \omega - \Omega$, where Ω is the group angular velocity, and putting $\psi = 0$. Therefore, $\dot{\boldsymbol{\theta}} = 0$ in Eq. (4) gives the stationary points as

$$\boldsymbol{\theta}^* = L^{\dagger}(\boldsymbol{\omega} + \boldsymbol{d}), \tag{5}$$

where $L^{\dagger}$ is the pseudoinverse of the Laplacian L, which is of the form

$$L^{\dagger} = \sum_{j=2}^{N} \lambda_j^{-1} \boldsymbol{v_j} \boldsymbol{v_j}^T, \tag{6}$$

where $0 = \lambda_1 < \lambda_2 \leqslant \cdots \leqslant \lambda_N$ are the eigenvalues of L and $\boldsymbol{v_j}$ $(j = 1, 2, \ldots, N)$ are the eigenvectors of L with respect to the eigenvalues λ_j.

The order parameter in Eq. (2) is then approximated as

$$r \approx 1 - \frac{\| \boldsymbol{\theta}^* \|^2}{2N}, \tag{7}$$

where

$$\begin{aligned} \| \boldsymbol{\theta}^* \|^2 &= \langle \boldsymbol{\theta}^*, \boldsymbol{\theta}^* \rangle \\ &= \langle L^{\dagger}(\boldsymbol{\omega} + \boldsymbol{d}), L^{\dagger}(\boldsymbol{\omega} + \boldsymbol{d}) \rangle \\ &= \sum_{j=2}^{N} \lambda_j^{-2} \langle \boldsymbol{v_j}, \boldsymbol{\omega} + \boldsymbol{d} \rangle^2. \end{aligned}$$

Now, by substituting the above expression in Eq. (7), we get the order parameter as

$$\begin{aligned} r &= 1 - \frac{1}{2N} \sum_{j=2}^{N} \lambda_j^{-2} \langle \boldsymbol{v_j}, \boldsymbol{\omega} + \boldsymbol{d} \rangle^2 \\ &= 1 - \frac{1}{2} J(\boldsymbol{\omega}, L), \end{aligned} \tag{8}$$

where $J(\boldsymbol{\omega}, L) = \frac{1}{N} \sum_{j=2}^{N} \lambda_j^{-2} \langle \boldsymbol{v_j}, \boldsymbol{\omega} + \boldsymbol{d} \rangle^2$ is known as synchrony alignment function. Here we note that in Eq. (8), the $J(\boldsymbol{\omega}, L) \to 0$ limit leads to $r = 1$, which denotes the perfect synchronization state. Therefore, for the achievement of perfect synchronization at a given point, we choose

$$\boldsymbol{\omega} + \boldsymbol{d} = 0. \tag{9}$$

Thus, the frequency set for the achievement of perfect synchronization at a targeted point in the parameter space is given by

$$\boldsymbol{\omega} = K_1^{(p)} \boldsymbol{k^{(1)}} \sin\alpha + K_2^{(p)} \boldsymbol{k^{(2)}} \sin\beta, \tag{10}$$

where $K_1^{(p)}$ and $K_2^{(p)}$ are the targeted coupling strength for pairwise and triadic interaction, respectively. We now proceed with the numerical verification of the proposed framework for achieving perfect synchronization at targeted coupling strengths for fixed phase-lags α and β, considering different networks.

IV. NUMERICAL VERIFICATION

The achievement of perfect synchronization in complex networks at a targeted point in the parameter space using the frequency set (analytically derived by the method described in the previous section) is numerically verified in this section.

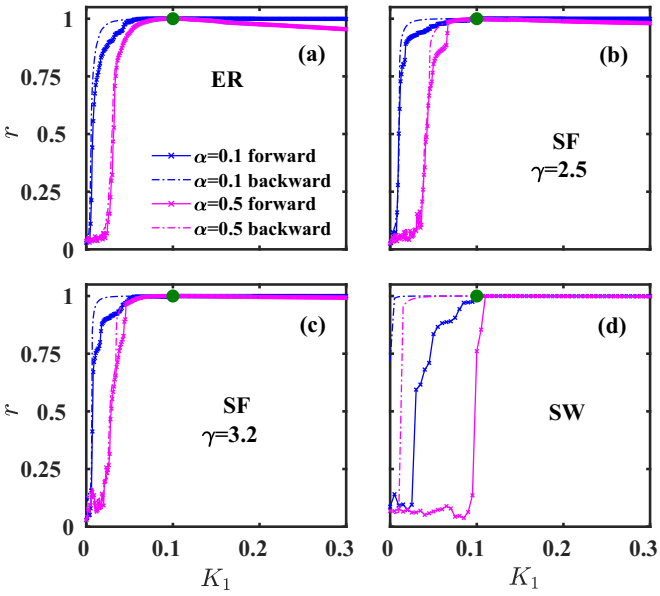

FIG. 1. Perfect synchronization for different networks. Numerically computed order parameter r as a function of pairwise coupling strength K_1 shown for phase lags $\alpha = 0.1$ (blue) and 0.5 (magenta). The triadic coupling K_2 is set to 0.5. The green dots indicate perfect synchronization states at targeted coupling $K_1 = 0.1$. (a) The ER network achieves $r = 1$ at $K_1 = 0.1$ in both forward and backward simulations. (b) and (c) The SF network with $\gamma = 2.5$ and 3.2 attains $r = 1$ at $K_1 = 0.1$ in both forward and backward simulations. (d) The SW network achieves perfect synchronization at $K_1 = 0.1$ in forward and backward simulations only for $\alpha = 0.1$. For the other lag, the backward path only attains $r = 1$.

For that purpose, we numerically simulate the Sakaguchi-Kuramoto model with higher-order interactions on top of four different complex networks of the same size ($N = 10^3$). The considered networks are one Erdős-Rényi (ER) [53–55] network; two scale-free (SF) [56] networks with exponents $\gamma = 2.5$ and 3.2; and one small-world (SW) [57] network. The SF network with exponent 2.5 is of mean degree $\langle k \rangle = 6$ and each of the other three networks have mean degree $\langle k \rangle = 8$. Numerical simulations are performed using the fourth-order Runge-Kutta method with step size $\delta t = 0.01$ for a sufficiently long time after removing the transients. For the next few numerical illustrations, we take $\alpha = \beta$ and set the target points at $K_1^{(p)} = 0.1$ and $K_2^{(p)} = 0.5$. In each case, we numerically continue the solutions in both forward and backward directions.

First we fix $K_2 = 0.5$ and vary K_1 around the target point $K_1^{(p)} = 0.1$ for the achievement of perfect synchronization in each of the considered networks for different values of $\alpha = \beta = 0.1$ and 0.5 (0.3 and 0.7 are shown in Fig. 12 in the Appendix). For each α, we use the frequency set derived by Eq. (10) and obtain the statistically steady solutions after integrating the system for a sufficiently long time. Although here we have chosen $\alpha = \beta$, using the derived frequency set, perfect synchronization can be achieved at a targeted point for $\alpha \neq \beta$. This fact is illustrated towards the end of this section.

Starting from $K_1 = 0$, the solution is then continued in the forward direction by changing the value of K_1 in small steps and using the last values of the phase variables of the previous

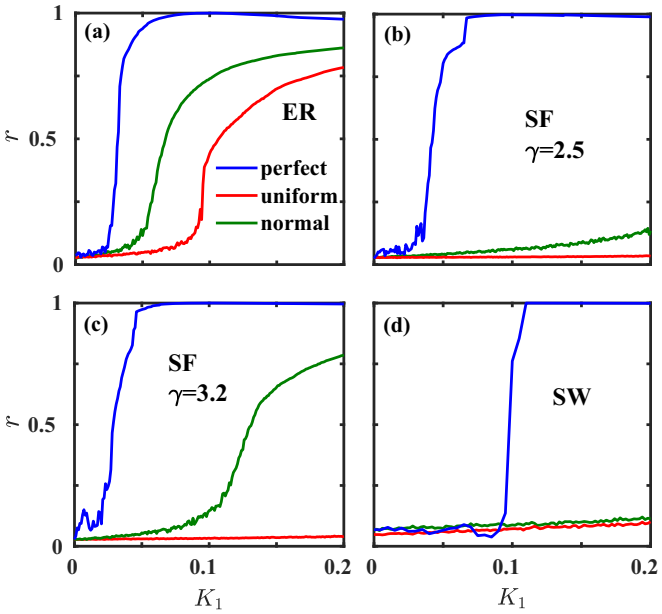

FIG. 2. Synchronization diagram for fixed $K_2 = \alpha = 0.5$ with natural frequencies drawn from the normal, uniform, and derived (perfect) frequency will ensure perfect synchronization at $K_1 = 0.1$ in different networks of size $N = 1000$: (a) r vs K_1 for the ER network; (b) and (c) r vs K_1 for the SF networks with $\gamma = 2.5$ and 3.2, respectively; and (d) r vs K_1 for the SW network. For the green, red, and blue curves in panels (a)–(d), the natural frequencies are drawn from the normal, uniform, and derived (perfect) frequency distributions, respectively.

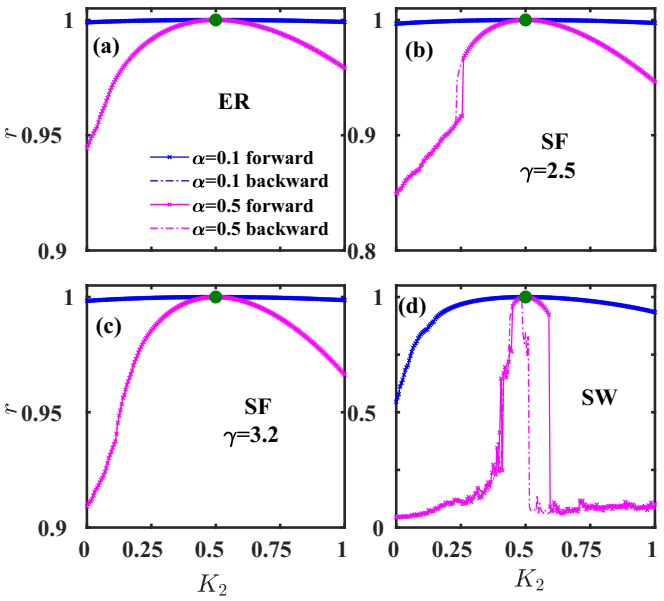

FIG. 3. Synchronization of the SK model with HOIs for different networks. Synchronization diagrams describe the order parameter r as a function of triadic coupling K_2 for fixed $K_1 = 0.1$. The blue and magenta curves present the transitions for $\alpha = 0.1$ and 0.5, respectively. The green dots denote the perfect synchronization states. (a) The ER network achieves $r = 1$ at $K_2 = 0.5$ for considered lags in both paths. (b) and (c) The SF networks with $\gamma = 2.5$ and 3.2 attain perfect synchronization at $K_2 = 0.5$ for considered α values in both paths. (d) The SW network attains $r = 1$ at $K_2 = 0.5$ only during forward transition (except $\alpha = 0.1$).

simulation as the initial condition for the present simulation. In the process, we continue the solution till $K_1 = 0.3$ and then continue the solution similarly in the backward direction by gradually reducing the value of K_1 in steps of $\delta K_1 = 0.001$ right up to the starting value of K_1. The variations of the synchronization order parameter (r) with K_1 for fixed $K_2 = 0.5$ obtained from the simulation data are shown in the Fig. 1. From Figs. 1(a), 1(b), and 1(c), one can observe that in the cases of the ER network and the SF networks with $\gamma = 2.5$ and 3.2, perfect synchronization is achieved at the targeted point (marked by a green dot) during forward as well backward continuation for all values of α. However, for the other case [Fig. 1(d)], perfect synchronization is achieved at the targeted point during backward continuation for all considered α, while for forward continuation it is achieved at the targeted point for lower values of α. Since prior studies with only pairwise interactions suggested that the frustration parameter had a negative impact on the hysteresis loop, this is an unexpected result in the presence of higher-order interactions [40]. It follows from the foregoing explanation that, given high values of the frustration parameter, perfect synchronization can be accomplished in a variety of networks using the analytically derived frequency set.

Further, the analytically derived frequency which has functional dependence on both the pairwise and the triadic interactions not only provides perfect synchronization at a targeted point in the parameter space but also helps in achieving a very high level of synchronization around the targeted point compared to other standard frequencies. Figure 2 shows the comparison of the level of synchronization in the considered networks for different frequency sets. Here, simulations are performed with uniform and normal frequencies along with the derived frequency set. In each case, the derived frequency set clearly provides a substantially higher level of synchronization around the targeted point.

Next we fix the pairwise coupling strength $K_1 = 0.1$ and vary the triadic coupling strength K_2 around the targeted point ($K_2^{(p)} = 0.5$) and perform numerical simulations using the SK model on the same complex networks considered above. As before, in this case also we numerically continue the solutions both in forward and backward directions by changing K_2 in the steps of $\delta K_2 = 0.005$ for different values of α. The variations of r with K_2 as obtained from the simulation data in different cases are shown in Fig. 3, which clearly shows the impact of triadic interaction in the system. It is observed that for all four networks perfect synchronization is achieved at the targeted coupling with different transition paths. The ER and SF networks show continuous transition to synchronization for small α. Whereas, at $\alpha = 0.7$ both of the SF networks exhibit a small window of hysteresis around the perfect synchronization point (see Fig. 13 in Appendix). For higher values of α, the system (phase-lag oscillators in SW network) gradually reaches to the highest point ($r = 1$), and then it sharply drops to 0. We have also observed that during the backward transition, the perfect as well as the higher degree of synchronization is achieved (near the targeted point) only for a small range of coupling. The reason is as follows: during the backward

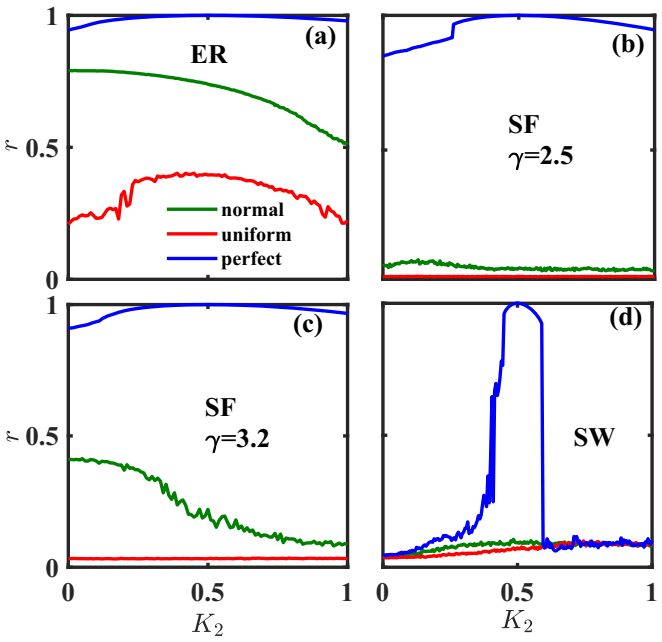

FIG. 4. Synchronization diagram for fixed $K_1 = 0.1$ and $\alpha = 0.5$ with natural frequencies drawn from the normal, uniform, and derived (perfect) frequency distributions for achieving perfect synchronization at $K_2 = 0.5$ in different networks of size $N = 1000$: (a) r vs K_2 for the ER network; (b) and (c) r vs K_2 for the SF networks with $\gamma = 2.5$ and 3.2, respectively; and (d) r vs K_2 for the SW network. The color convention is same as the one used in Fig. 2.

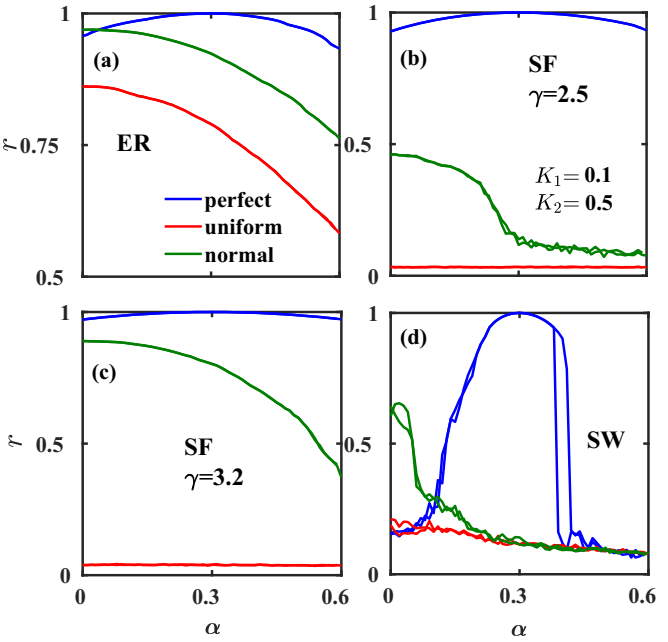

FIG. 5. Synchronization diagram for fixed $K_1 = 0.1$ and $K_2 = 0.5$ with natural frequencies drawn from the normal, uniform, and derived (perfect) frequency distributions for achieving perfect synchronization at $\alpha = 0.3$ in different networks of size $N = 1000$: (a) r vs α for the ER network; (b) and (c) r vs α for the SF networks with $\gamma = 2.5$ and 3.2, respectively; and (d) r vs α for the SW network. The color convention is same as the one used in Fig. 2.

transition, the system is already in fully incoherent states, and thus, it tries to remain in the incoherent state if we decrease the coupling strength. However, when it comes closer to $K_2^{(p)} = 0.5$, the coupling-strength-dependent frequency drives the entire system to reach the perfect (or near perfect) synchronization regime. A further decrease of coupling strength reduces the level or degree of synchronization and drives the entire system to be fully desycnhronized. These results confirm that using the analytically derived frequency set one can achieve a perfectly synchronized state either in the forward transition path or in the backward transition path. Subsequently, we analyze the analytically derived frequency set.

At this point let us recall that the derived frequency set promotes a very high level of synchronization around the targeted point as the pairwise coupling strength K_1 varies for fixed targeted triadic coupling strength (see Fig. 2). Next, to check for the similar behavior of the level of synchronization, we perform simulations by varying K_2 around the targeted point for fixed $K_1 = 0.1$. Figure 4 shows that in this case also the derived frequency provides a very high level of synchronization compared to other frequency sets. Finally, for fixed K_1 and K_2, we check the achievement of perfect synchronization at a targeted value of the phase frustration. Thus, we set $K_1 = 0.1$ and $K_2 = 0.5$, and we derive the frequency set from Eq. (10) for achieving perfect synchronization at $\alpha = 0.3$. Using this derived frequency set, numerical simulation of the network is performed and the variation of the order parameter (r) with the phase lag (α) is computed and is shown in Fig. 5. From the figure, one can clearly observe that perfect synchrony is achieved at the targeted phase frustration $\alpha = 0.3$. In Fig. 5, apart from the variation of r with α (blue curve) for the derived frequency, the same variation of r with α have been shown also for the other two frequency sets showing very low levels of synchronization compared to the derived one. Although, in the preceding discussion, we have used networks of size $N = 1000$, the proposed framework is independent of the network size N and we have verified it for larger networks in some test cases.

Now, to understand the contributions of pairwise and triadic interactions in the derived frequency for achieving perfect synchronization at a targeted point, we analyze the frequency distributions corresponding to the pairwise ($\boldsymbol{\omega_1} = K_1^{(p)}\boldsymbol{k^{(1)}}\sin\alpha$) and triadic interactions ($\boldsymbol{\omega_2} = K_2^{(p)}\boldsymbol{k^{(2)}}\sin\alpha$) in the expression (10) along with the total derived frequency distribution. Figure 6 shows the distribution of the derived frequency for perfect synchronization from Eq. (10) for four different networks of size $N = 1000$ and two phase-lag values (0.1 and 0.7). The figure also displays the distributions of $\boldsymbol{\omega_1}$ and $\boldsymbol{\omega_2}$ separately in the insets of each panel. It is observed that the range of the frequencies increases substantially with lag. As the sets $\boldsymbol{\omega_1}$ and $\boldsymbol{\omega_2}$ are linearly correlated with the pairwise degree $\boldsymbol{k^{(1)}}$ and the triadic degree $\boldsymbol{k^{(2)}}$, the distributions also look like the distribution of the pairwise and triadic degrees, respectively. Since the ER network has a small number of triangles, from the distribution of $\boldsymbol{\omega_2}$ it is clear that the effect of triangular interactions is less than the effect of pairwise interactions [Figs. 6(a) and 6(b)]. For the SF networks also there are more pairwise interactions than triadic interactions [Figs. 6(c)–6(f)]. For these networks perfect synchronization is attained at the targeted coupling even for large phase-lag

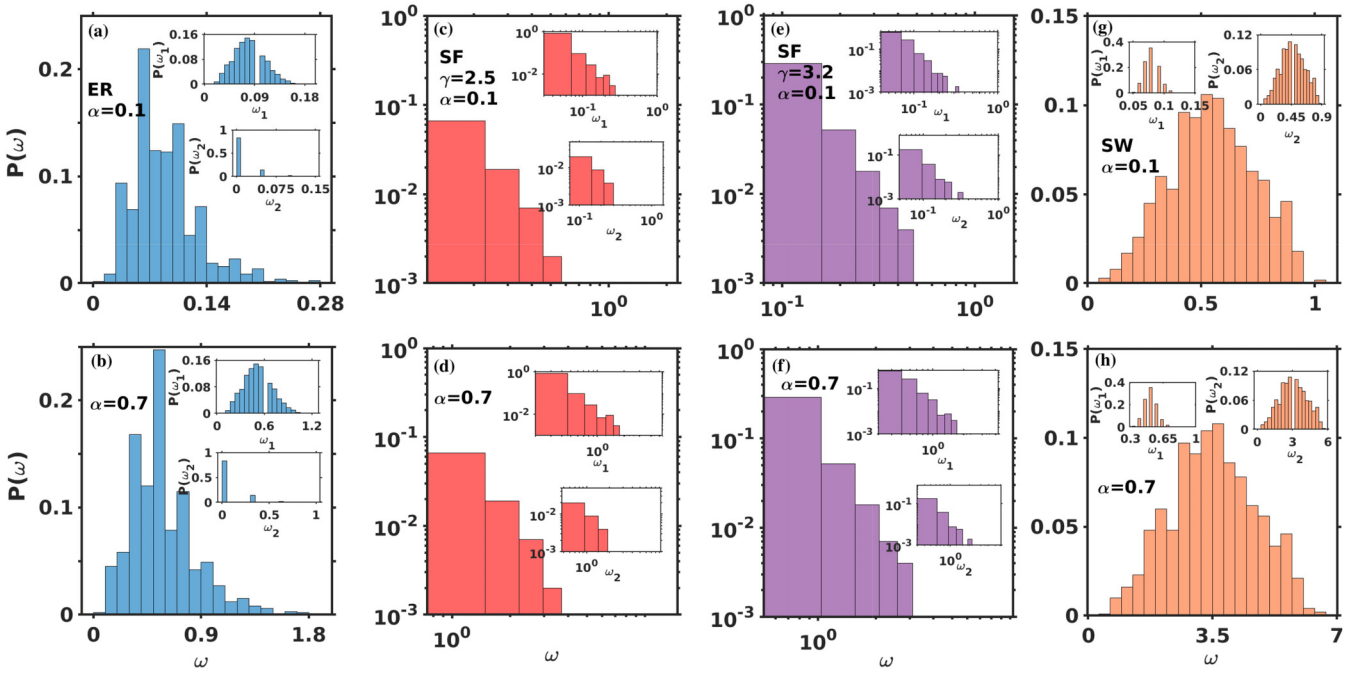

FIG. 6. Distribution of the frequency for perfect synchronization using the four different networks, namely, (a) and (b) ER (blue); (c) and (d) SF with $\gamma = 2.5$ (red); (e) and (f) SF with $\gamma = 3.2$ (purple); and (g) and (h) SW (brown), of network size $N = 1000$. In the first row the frequency is calculated for the phase lag $\alpha = 0.1$ and in the second row it is calculated for the phase lag $\alpha = 0.7$. We take the pairwise coupling strength $K_1^{(p)} = 0.1$ and the higher-order coupling strength $K_2^{(p)} = 0.5$.

values. Only in the case of the SW network there are a higher number of triadic interactions [Figs. 6(g) and 6(h)], which is a reason the effect of triadic interaction in the constructed frequency is much higher compared to that of the ER or SF networks. This effect of triadic interaction increases the heterogeneity in the system and prevents the system from synchronizing [58], although the predicted frequency is able to overcome this constraint and reach the global synchrony for a small vicinity of the parameter space. Note that the derived

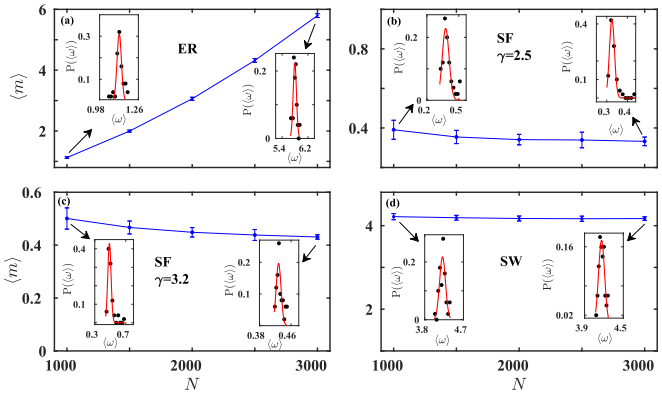

FIG. 7. Distribution of mean of average frequencies over 50 realizations of networks is shown as a function of network size for (a) the ER network; (b) and (c) the SF networks with $\gamma = 2.5$ and 3.2, respectively; and (d) the SW network. The error bars represents the standard deviation over 50 realizations of networks and the dots on the blue curve represents the mean of the same. The insets represent the distribution of the mean of average frequencies of network sizes $N = 1000$ and 3000.

frequency is dependent on the considered connectivity network. Changing the network structure will lead to the change in the derived frequency set. However, we have plotted the frequency distribution of $\boldsymbol{\omega}$ for network size $N = 5000$ across 100 realizations to give an idea of how the distribution of the frequency will appear for networks with large size (see Fig. 14 in appendix).

Now we investigate the properties of the derived frequency sets in more detail. For that purpose, the network sizes of all four networks considered here are varied from 1000 to 3000. Fifty networks of each type and size are generated, and the frequency is calculated taking the values $K_1 = 0.1$, $K_2 = 0.5$, and $\alpha = 0.5$. In each case we calculate the average $\langle m \rangle = \frac{1}{50} \sum_{i=1}^{50} \langle \boldsymbol{\omega} \rangle$ and the standard deviation of the mean frequencies. The $\boldsymbol{\omega}$ depends on the structure of the graph, and for each realization a new $\boldsymbol{\omega}$ will be generated. We do statistical analysis to check whether there will be strong variability of these generated frequency sets. For each form of network that was taken into consideration, Fig. 7 displays the changes in mean and standard deviation. We see that for ER networks [Fig. 7(a)], the mean of the average frequency grows with the number of nodes, whereas for SF networks, the mean of the average frequency declines with a very modest slope. Note that, in the case of ER networks, the connection probability of the ER network is kept fixed, and as a result the mean degree is increased with the network size. On the other hand, for SF networks the minimum degree of the networks is kept fixed and for SW networks the average degree of the networks is kept approximately the same across all sizes of networks. In the case of SW networks, the mean of the average frequency almost remains the same for any significant change in the size of the networks [Fig. 7(d)]. The

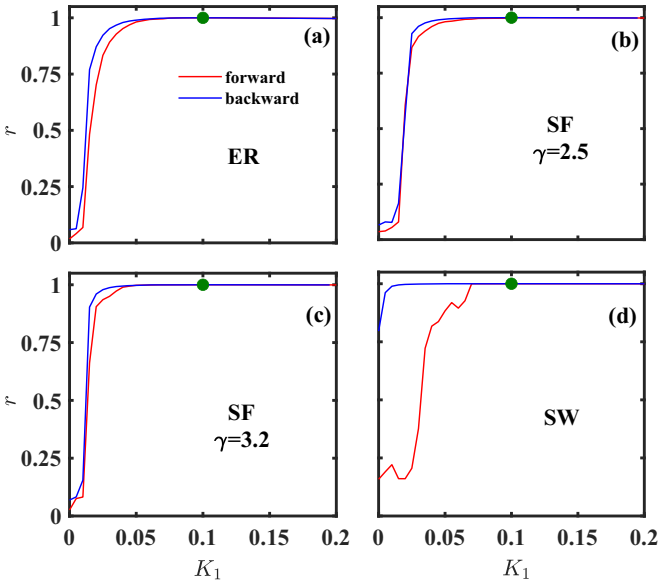

FIG. 8. Synchronization profile for the derived frequency set for $\alpha = 0.2$, $\beta = 0.1$, $K_1 = 0.1$, and $K_2 = 0.5$ for different networks of size $N = 1000$: (a) r vs K_1 for the ER network; (b) and (c) r vs K_1 for the SF networks with $\gamma = 2.5$ and 3.2, respectively; and (d) r vs K_1 for the SW network. The green dots show the perfect synchronization states at the targeted coupling $K_1 = 0.1$ for all the networks.

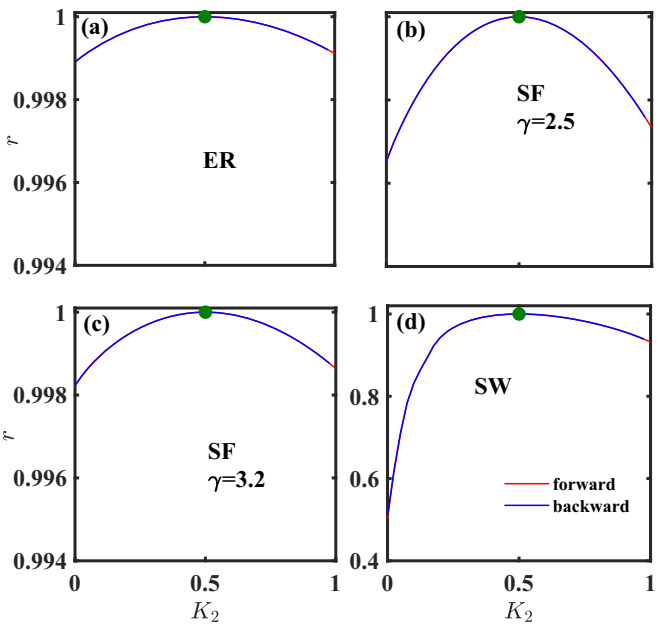

FIG. 9. Synchronization profile for the derived frequency set for $\alpha = 0.2$, $\beta = 0.1$, $K_1 = 0.1$, and $K_2 = 0.5$ for different networks of size $N = 1000$: (a) r vs K_2 for the ER network, (b) and (c) r vs K_2 for the SF networks with $\gamma = 2.5$ and 3.2, respectively; and (d) r vs K_2 for the SW network. All considered networks attain $r = 1$ (green dot) at the targeted point $K_2 = 0.5$ for both forward (red) and backward (blue) continuation.

error bars in the figures represent the standard deviations over 50 realizations. The dots in the insets represent the distribution of the average frequency over 50 realizations of networks of sizes $N = 1000$ and $N = 3000$, respectively and the curves are the best Gaussian fits for those points. The observation suggests (less variation around the mean frequencies) that the generated frequencies are not changing drastically if the network size and link density remain fixed.

As mentioned earlier, although we have presented all the results by setting $\alpha = \beta$, the proposed scheme works in the general case where $\alpha \neq \beta$. To check that, we take $\alpha = 0.2$ and $\beta = 0.1$ and perform the numerical simulation to achieve perfect synchronization for $K_1^{(p)} = 0.1$ and $K_2^{(p)} = 0.5$ using the derived frequency set given by Eq. (10). Figure 8 shows the variation of the order parameter computed from the simulation data around the targeted point $K_1 = 0.1$ for fixed $K_2 = 0.5$ for four considered networks. Also the variations of r with K_2 around the targeted point for fixed $K_1 = 0.1$ for these networks are shown in Fig. 9. From these two figures also the achievement of perfect synchronization at the targeted point for different phase-lags associated with the pairwise and triadic interactions is quite apparent. Next we perform low-dimensional reduction of the system to understand the stability of the achieved synchronization state using the derived frequency set.

V. LOW-DIMENSIONAL REDUCTION

To analyze the stability of the synchronized state around the targeted parameter values, we reduce the networked system in Eq. (1) to its low-dimensional form using the collective coordinate approach [49,59,60]. In this approach the phase of each oscillator is approximated by its intrinsic frequency using

$$\theta_i(t) = \chi(t)\omega_i, \tag{11}$$

where $\chi(t)$ is the collective coordinate, which is time dependent. To ensure the validity of this approach, we aim to minimize the error given by

$$\epsilon_i(\chi) = \dot{\chi}\omega_i - \omega_i - K_1 \sum_{j=1}^{N} A_{ij} \sin[\chi(\omega_j - \omega_i) - \alpha] - \frac{K_2}{2} \sum_{j=1}^{N} \sum_{l=1}^{N} B_{ijl} \sin[\chi(2\omega_j - \omega_l - \omega_i) - \beta]. \tag{12}$$

This error will be minimum if it is orthogonal to the tangent space of the solution space given by Eq. (11), which is spanned by $\frac{\partial \theta_i}{\partial \chi} = \omega_i$ [59,60]. Now, projecting this error to the specified subspace and using the orthogonality property, we obtain a one-dimensional evolution equation for $\chi(t)$,

$$\frac{d\chi}{dt} = g(\chi), \tag{13}$$

where $g(\chi)$ is given by

$$g(\chi) = 1 + \frac{K_1}{\sigma^2} \sum_{i=1}^{N} \omega_i \sum_{j=1}^{N} A_{ij} \sin[\chi(\omega_j - \omega_i) - \alpha] + \frac{K_2}{2\sigma^2} \sum_{i=1}^{N} \omega_i \sum_{j=1}^{N} \sum_{l=1}^{N} B_{ijl} \sin[\chi(2\omega_j - \omega_l - \omega_i) - \beta] \tag{14}$$

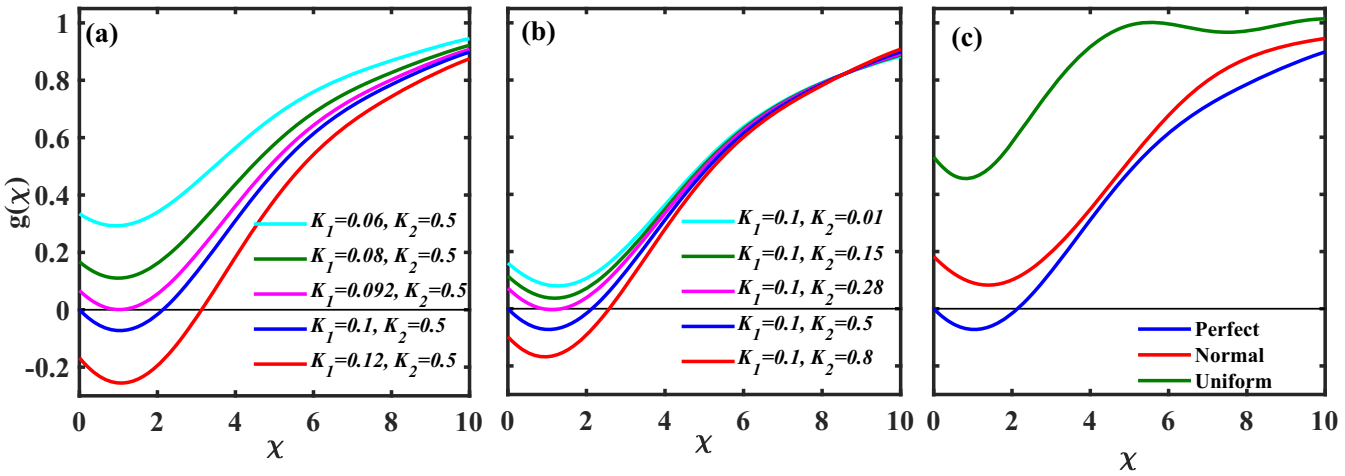

FIG. 10. Variation of g obtained in Eq. (14) as a function of χ under derived frequency for the ER network. (a) Coupling K_2 is set to 0.5 and the values of K_1 are taken as 0.06 (cyan), 0.08 (green), 0.092 (magenta), 0.1 (blue), and 0.12 (red). (b) Coupling K_1 is fixed to 0.1 and the value of K_2 varies as 0.01 (cyan), 0.15 (green), 0.28 (magenta), 0.5 (blue), and 0.8 (red). (c) Derived (perfect) frequency (blue) and normally (red), and uniformly (green) distributed frequencies are plotted, showing that only the derived frequency reaches the stable synchronization state.

and $\sigma^2 = \sum_{i=1}^{N} \omega_i^2$. The one-dimensional differential Eq. (13) will have a stable equilibrium if $g(\chi) = 0$ and $g'(\chi) < 0$. At the equilibrium, χ is independent of time and hence Eq. (11) indicates that all θ_i's will be time independent, which implies the system will exhibit a phase-locked solution. If such a fixed point occurs at $\chi = 0$, all phases will be 0, resulting in perfect synchronization.

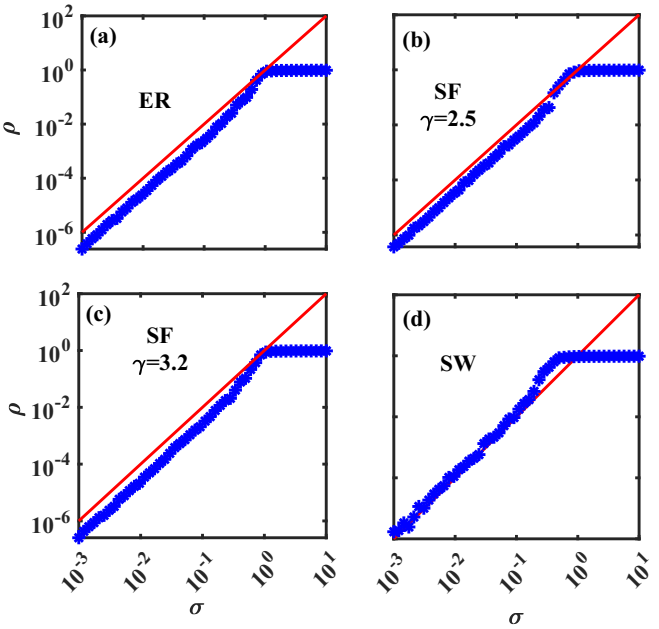

FIG. 11. Synchronization error (ρ) under deviated frequency in different networks of size $N = 1000$: (a) ρ vs σ in the ER network; (b) and (c) ρ vs σ in the SF networks with $\gamma = 2.5$ and 3.2, respectively; and (d) ρ vs σ in the SW network. The data represented by the blue stars are obtained from numerical simulation, and the red lines represent the analytically obtained function $\rho \sim \sigma^2$.

In Figs. 10(a) and 10(b), we show the behavior of $g(\chi)$ under derived frequency for perfect synchronization $\boldsymbol{\omega}$ (targeted at $K_1 = 0.1$ and $K_2 = 0.5$, respectively), for a set of values of K_1 and K_2 in the ER network. We now fix K_1 to 0.1 and vary K_2 in Fig. 10(b). For $K_2 = 0.01$ and 0.15, $g(\chi)$ does not intersect $g(\chi) = 0$. Here, $g(\chi)$ touches the line $g(\chi) = 0$ for the first time at $K_2 = 0.28$, which provides a stable phase-locked solution. From this value of K_2 onward, $g(\chi)$ crossed the line $g(\chi) = 0$ with a negative slope, which indicates that the system has a stable phase-locked solution [as seen in Fig. 3(a)]. As per expectation the system exhibits perfect synchronization at $K_2 = 0.5$ [$g(\chi) = 0$ and $g'(\chi) < 0$ at $\chi = 0$]. For larger values of K_2 the synchronization remains stable. We do the analysis for the other two networks (SF and SW), which we found to be very similar.

In Fig. 10(a), we fixed K_2 to 0.5 and chose K_1 as 0.06, 0.08, 0.092, 0.1, and 0.12. For $K_1 = 0.06$ and 0.08, $g(\chi)$ does not intersect $g(\chi) = 0$; i.e., stable synchronization is not achieved at this point. At 0.092, $g(\chi)$ touches $g(\chi) = 0$, which means stable synchronization occurs for the first time. As the K_1 value increases from 0.092, the crossing point tends to 0, and finally at $K_1 = 0.1$ (targeted value), $g(\chi)$ is 0 and $g'(\chi) < 0$ at $\chi = 0$; i.e., the perfect synchronization is obtained. For the values of $K_1 > 0.1$ (0.12) the solution remains stable, as we see in Fig. 1(a).

Figure 10(c) shows the relation between χ and $g(\chi)$ for three types of natural frequency $\boldsymbol{\omega}$, namely, frequency for perfect synchronization, normally distributed frequency, and uniformly distributed frequency. Here the considered network is the ER network. We find that the choice of $\boldsymbol{\omega}$ which induces perfect synchronization, derived in Eq. (10), gives stable equilibrium at $\chi = 0$. For the other two frequency sets (normal and uniform distributed), $g(\chi)$ never intersects $g(\chi) = 0$. This shows that the synchronization is stable only for the choice of frequency set derived in Eq. (10) among the considered sets of frequencies.

VI. ROBUSTNESS OF THE FREQUENCY SET

The robustness of the derived frequency set ($\boldsymbol{\omega}$) for perfect synchronization is now checked by adding a perturbation to $\boldsymbol{\omega}$ in the form of Gaussian noise such that $\omega_i = \omega_i + \delta\omega_i$, where $\delta\omega_i$ is drawn from a normal distribution, $N(0, \sigma\omega_i)$, whose mean is 0 and standard deviation is $\sigma\omega_i$, which represents the multiplicative noise proportional to ω_i. Due to the effect of the perturbation in the optimal frequency, the system will deviate from the perfect synchronized state. We define this deviation from synchronization state as synchronization loss and define it as $\rho = 1 - r$, where r is the synchronization order parameter defined in Eq. (2). Now, from Eq. (7) we get

$$\rho = \frac{1}{2N} \parallel \boldsymbol{\theta} \parallel^2 \sim \frac{1}{2}\mathrm{Var}(\boldsymbol{\theta}), \tag{15}$$

where $\mathrm{Var}(\boldsymbol{\theta})$ denotes the variance of $\boldsymbol{\theta}$. Substituting the perturbed $\boldsymbol{\omega}$ in Eq. (5), we obtain

$$\boldsymbol{\theta} = L^{\dagger}\delta\boldsymbol{\omega}.$$

Since $L^{\dagger}$ and $\delta\boldsymbol{\omega}$ are approximately independent of each other, we can write

$$\mathrm{Var}(\boldsymbol{\theta}) = (L^{\dagger})^2\mathrm{Var}(\delta\boldsymbol{\omega}) = (L^{\dagger})^2\boldsymbol{\omega}^2\sigma^2. \tag{16}$$

The above equation confirms that $\mathrm{Var}(\boldsymbol{\theta}) \propto \sigma^2$, where the proportion constant is $(L^{\dagger})^2\boldsymbol{\omega}^2$, which is independent of σ. Using this fact, we reach a relation between $\mathrm{Var}(\boldsymbol{\theta})$ and σ as $\mathrm{Var}(\boldsymbol{\theta}) \sim \sigma^2$. Therefore, from Eq. (15) we get

$$\rho \sim \sigma^2. \tag{17}$$

A numerical verification is done in Fig. 11 using four networks, namely, the ER network, the SF networks with two exponents ($\gamma = 2.5$ and 3.2), and the SW network. It presents ρ as a function of σ. In all four cases, this figure shows that, for small σ, ρ is small, which means the deviation from synchronization is small when the deviation of the frequency from the designed frequency set is small. As the value of σ increases (the deviation from the derived frequency set increases), ρ also increases following the rule derived in Eq. (17). After a certain value of σ, the value of ρ saturates at 1 because at this stage the high deviation in the frequency set leads to a complete incoherent state (desynchronized state) with $r \to 0$, which leads to $\rho \to 1$.

VII. DISCUSSION

In this article, we study perfect synchronization in SK oscillators with higher-order interactions at considerably lower coupling strength. Adapting the framework developed in Ref. [39] we construct a set of natural frequencies that ensure perfect synchronization in the presence of HOIs. We presented a synchrony alignment function that measures the interplay between network structure and oscillator heterogeneity and allows us to get a set of frequencies for perfect synchronization. Focusing on the Sakaguchi-Kuramoto model with higher-order interactions, we described the effect of pairwise coupling as well as higher-order coupling

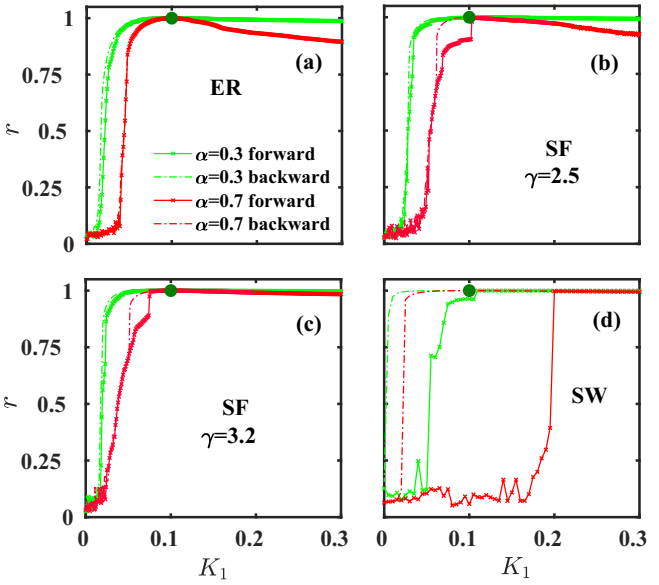

FIG. 12. Order parameter r is plotted as a function of pairwise coupling K_1 for $K_2 = 0.5$ and $\alpha = 0.3$ and 0.7. The green dots denote the perfect synchronization states. (a) The ER network attains $r = 1$ at targeted coupling $K_1 = 0.1$ in both forward and backward paths. (b) The SF network with $\gamma = 2.5$ attains $r = 1$ at $K_1 = 0.1$ except in the forward path for $\alpha = 0.7$. (c) The SF with $\gamma = 3.2$ achieves perfect synchronization at $K_1 = 0.1$ for considered lag values in both paths. (d) The SW network achieves perfect synchronization at $K_1 = 0.1$ in the backward paths only.

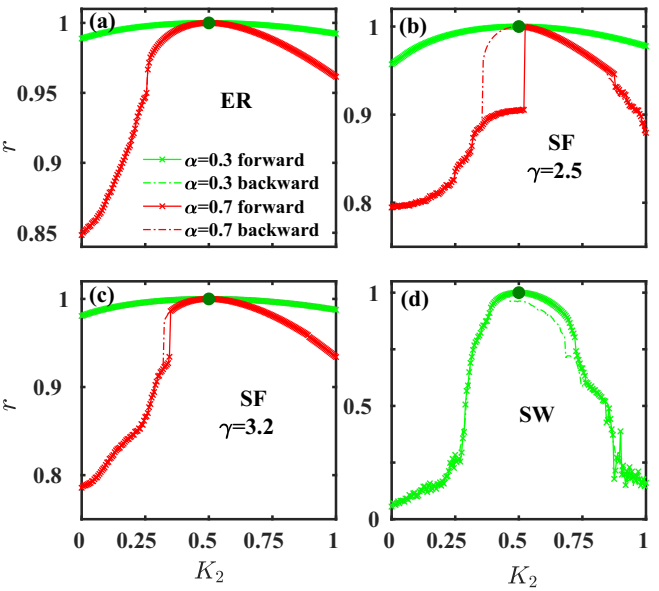

FIG. 13. Order parameter r is plotted as a function of higher-order coupling K_2 for $K_1 = 0.1$ and $\alpha = 0.3$ and 0.7. The green dots denote the perfect synchronization states. (a) The ER network shows perfect synchronization at predicted coupling $K_2 = 0.5$ in both forward and backward directions. (b) The SF network with $\gamma = 2.5$ attains $r = 1$ at $K_2 = 0.5$ except in the forward path for lag value 0.7. (c) The SF network with $\gamma = 3.2$ achieves perfect synchronization at $K_2 = 0.5$ for considered lag values in both paths. (d) The SW network achieves $r = 1$ at $K_2 = 0.5$ in the forward path only for $\alpha = 0.3$.

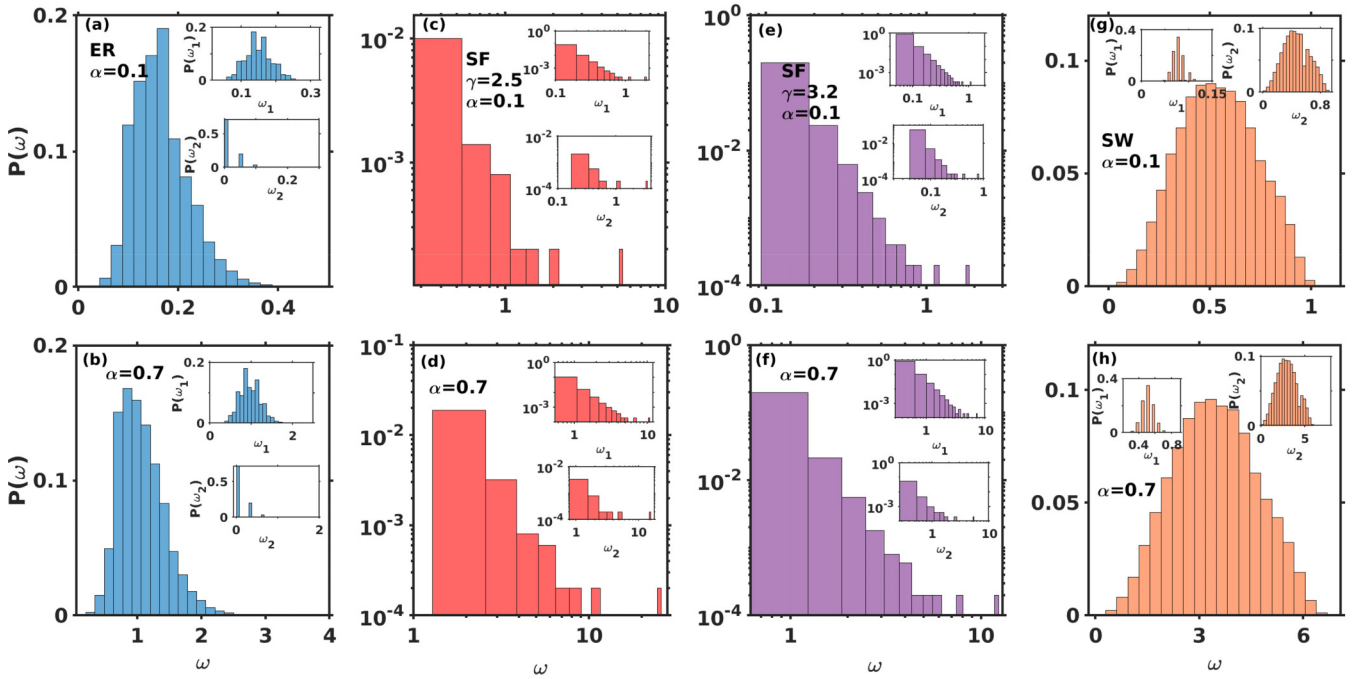

FIG. 14. Distribution of the derived frequency using the four different networks, namely, (a) and (b) ER (blue); (c) and (d) SF with $\gamma = 2.5$ (red); (e) and (f) SF with $\gamma = 3.2$ (purple); and (g) and (h) SW (brown), taking the average across 100 realizations of network size 5000 in each case. In the first row the frequency is calculated for phase lag $\alpha = 0.1$, and in the second row it is calculated for phase lag $\alpha = 0.7$. The pairwise coupling strength is set to $K_1^{(p)} = 0.1$ and the higher-order coupling strength is set to $K_2^{(p)} = 0.5$.

to reach the perfectly synchronized state at a targeted coupling strength for four different types of networks. We found that the analytically derived natural frequencies involve both structural and dynamical information of the phase-frustrated Kuramoto model with higher-order interactions. The synchronization is promoted by a strong alignment of the frequency vector with the most dominant Laplacian eigenvectors and the pseudoinverse operator. In all the cases, we found that our derived frequency can help the oscillators to reach the perfectly synchronized state, whereas any other frequency set does not reach the perfect synchronization state even with much higher coupling strength. Later, we derive a low-dimensional model to analyze the stability of the perfectly synchronized state using the collective coordinate approach. This provides a clear understanding of the stability of the synchronization state at different coupling strengths and with different frequency sets. We also checked the robustness of the derived frequency $\boldsymbol{\omega}$ by adding a small perturbation in the form of Gaussian noise. This shows that, even when we add some noise in the derived frequency set, the synchronization state is not lost unless the frequency deviation is too high.

The codes are available at Ref. [61].

ACKNOWLEDGMENTS

S.D. is supported by the INSPIRE program of the DST, India (Code No. IF190605). C.H. was supported by INSPIRE-Faculty grant (Code: IFA17-PH193).

APPENDIX

Figure 12 shows the variation of order parameter r with the pairwise coupling strength K_1 for $\alpha = 0.3, 0.7$. The order parameter shows small hysteresis region near the point of perfect synchronization for SF networks with $\alpha = 0.7$. For SW network hysteresis is observed with both $\alpha = 0.3, 0.7$. On the other hand, the order parameter r as a function of higher order coupling strength K_2 is shown in Fig. 13. We observe that a hysteresis window exist near the desired perfect synchronization point for SF networks at $\alpha = 0.7$.

To understand the frequency distribution for larger networks, we have considered networks with size $N = 5000$ across 100 realizations and plot the distribution of the derived frequency in Fig. 14.

[1] S. Majhi, M. Perc, and D. Ghosh, J. R. Soc., Interface **19**, 20220043 (2022).
[2] F. Battiston, G. Cencetti, I. Iacopini, V. Latora, M. Lucas, A. Patania, J.-G. Young, and G. Petri, Phys. Rep. **874**, 1 (2020).
[3] G. Petri, S. Musslick, B. Dey, K. Özcimder, D. Turner, N. K. Ahmed, T. L. Willke, and J. D. Cohen, Nat. Phys. **17**, 646 (2021).
[4] U. Alvarez-Rodriguez, F. Battiston, G. F. de Arruda, Y. Moreno, M. Perc, and V. Latora, Nat. Hum. Behav. **5**, 586 (2021).
[5] I. Iacopini, G. Petri, A. Barrat, and V. Latora, Nat. Commun. **10**, 2485 (2019).
[6] A. Kumar, S. Chowdhary, V. Capraro, and M. Perc, Phys. Rev. E **104**, 054308 (2021).

[7] S. Panahi, F. Nazarimehr, S. Jafari, J. C. Sprott, M. Perc, and R. Repnik, Appl. Math. Comput. **394**, 125830 (2021).

[8] F. Parastesh, K. Rajagopal, S. Jafari, M. Perc, and E. Schöll, Phys. Rev. E **105**, 054304 (2022).

[9] F. Parastesh, M. Mehrabbeik, K. Rajagopal, S. Jafari, and M. Perc, Chaos **32**, 013125 (2022).

[10] L. Martignon, H. Von Hassein, S. Grün, A. Aertsen, and G. Palm, Biol. Cybern. **73**, 69 (1995).

[11] S. Yu, H. Yang, H. Nakahara, G. S. Santos, D. Nikolić, and D. Plenz, J. Neurosci. **31**, 17514 (2011).

[12] C. Giusti, R. Ghrist, and D. S. Bassett, J. Comput. Neurosci. **41**, 1 (2016).

[13] M. W. Reimann, M. Nolte, M. Scolamiero, K. Turner, R. Perin, G. Chindemi, P. Dłotko, R. Levi, K. Hess, and H. Markram, Front. Comput. Neurosci. **11**, 48 (2017).

[14] A. E. Sizemore, C. Giusti, A. Kahn, J. M. Vettel, R. F. Betzel, and D. S. Bassett, J. Comput. Neurosci. **44**, 115 (2018).

[15] S. Chatterjee, S. Nag Chowdhury, D. Ghosh, and C. Hens, Chaos **32**, 103122 (2022).

[16] J. Grilli, G. Barabás, M. J. Michalska-Smith, and S. Allesina, Nature (London) **548**, 210 (2017).

[17] E. Bairey, E. D. Kelsic, and R. Kishony, Nat. Commun. **7**, 12285 (2016).

[18] G. Petri, P. Expert, F. Turkheimer, R. Carhart-Harris, D. Nutt, P. J. Hellyer, and F. Vaccarino, J. R. Soc., Interface **11**, 20140873 (2014).

[19] C. Giusti, E. Pastalkova, C. Curto, and V. Itskov, Proc. Natl. Acad. Sci. U.S.A. **112**, 13455 (2015).

[20] E. Ganmor, R. Segev, and E. Schneidman, Proc. Natl. Acad. Sci. U.S.A. **108**, 9679 (2011).

[21] L. V. Gambuzza, F. Di Patti, L. Gallo, S. Lepri, M. Romance, R. Criado, M. Frasca, V. Latora, and S. Boccaletti, Nat. Commun. **12**, 1255 (2021).

[22] P. S. Skardal and A. Arenas, Phys. Rev. Lett. **122**, 248301 (2019).

[23] S. Ghosh, P. Khanra, P. Kundu, P. Ji, D. Ghosh, and C. Hens, Chaos **33**, 053117 (2023).

[24] S. Strogatz, *Sync: The Emerging Science of Spontaneous Order* (Penguin UK, London, 2004).

[25] A. Pikovsky, M. Rosenblum, J. Kurths, and J. Kurths, *Synchronization: A Universal Concept in Nonlinear Sciences*, Cambridge Nonlinear Science Series, Vol. 12 (Cambridge University, Cambridge, England, 2003).

[26] Y. Kuramoto, *Chemical Oscillations, Waves, and Turbulence* (Dover, Mineola, NY, 2003).

[27] M. Newman, *Networks: An Introduction* (Oxford University, Oxford, 2010).

[28] R. Cohen and S. Havlin, *Complex Networks: Structure, Robustness and Function* (Cambridge University, Cambridge, England, 2010).

[29] A. Barrat, M. Barthelemy, and A. Vespignani, *Dynamical Processes on Complex Networks* (Cambridge University, Cambridge, England, 2008).

[30] Y. Kuramoto, *Chemical Oscillations, Waves, and Turbulence* (Springer, Berlin, 1984), pp. 111–140.

[31] J. A. Acebrón, L. L. Bonilla, C. J. P. Vicente, F. Ritort, and R. Spigler, Rev. Mod. Phys. **77**, 137 (2005).

[32] J. Gómez-Gardeñes, S. Gómez, A. Arenas, and Y. Moreno, Phys. Rev. Lett. **106**, 128701 (2011).

[33] I. Leyva, R. Sevilla-Escoboza, J. M. Buldú, I. Sendiña-Nadal, J. Gómez-Gardenes, A. Arenas, Y. Moreno, S. Gómez, R. Jaimes-Reategui, and S. Boccaletti, Phys. Rev. Lett. **108**, 168702 (2012).

[34] Jesús Gómez-Gardeñes, Y. Moreno, and A. Arenas, Phys. Rev. Lett. **98**, 034101 (2007).

[35] X. Zhang, S. Boccaletti, S. Guan, and Z. Liu, Phys. Rev. Lett. **114**, 038701 (2015).

[36] B. C. Coutinho, A. V. Goltsev, S. N. Dorogovtsev, and J. F. F. Mendes, Phys. Rev. E **87**, 032106 (2013).

[37] T. Ichinomiya, Phys. Rev. E **70**, 026116 (2004).

[38] P. R. Chamlagai, D. Taylor, and P. S. Skardal, Phys. Rev. E **106**, 034202 (2022).

[39] P. Kundu, C. Hens, B. Barzel, and P. Pal, Europhys. Lett. **120**, 40002 (2017).

[40] P. Kundu, P. Khanra, C. Hens, and P. Pal, Phys. Rev. E **96**, 052216 (2017).

[41] P. Kundu, P. Khanra, C. Hens, and P. Pal, Europhys. Lett. **129**, 30004 (2020).

[42] P. Kundu and P. Pal, Chaos **29**, 013123 (2019).

[43] H. Sakaguchi and Y. Kuramoto, Prog. Theor. Phys. **76**, 576 (1986).

[44] P. S. Skardal, D. Taylor, J. Sun, and A. Arenas, Phys. Rev. E **91**, 010802(R) (2015).

[45] P. S. Skardal and A. Arenas, Commun. Phys. **3**, 218 (2020).

[46] Y. Cui, S. Ahmad, and J. Hawkins, Front. Comput. Neurosci. **11**, 111 (2017).

[47] P. S. Skardal, L. Arola-Fernández, D. Taylor, and A. Arenas, Phys. Rev. Res. **3**, 043193 (2021).

[48] O. E. Omel'chenko and M. Wolfrum, Phys. Rev. Lett. **109**, 164101 (2012).

[49] M. Brede and A. C. Kalloniatis, Phys. Rev. E **93**, 062315 (2016).

[50] P. Khanra, P. Kundu, P. Pal, P. Ji, and C. Hens, Chaos **30**, 031101 (2020).

[51] P. S. Skardal, D. Taylor, and J. Sun, Phys. Rev. Lett. **113**, 144101 (2014).

[52] S. Adhikari, J. G. Restrepo, and P. S. Skardal, Chaos **33**, 033116 (2023).

[53] P. Erdős and A. Rényi, Publ. Math. (Debrecen) **6**, 290 (1959).

[54] P. Erdős and A. Rényi, Publ. Math. Inst. Hung. Acad. Sci. **5**, 17 (1960).

[55] P. Erdős and A. Rényi, Acta Math. Hung. **12**, 261 (1964).

[56] A.-L. Barabási and E. Bonabeau, Sci. Am. **288**, 60 (2003).

[57] D. J. Watts and S. H. Strogatz, Nature (London) **393**, 440 (1998).

[58] M. Chutani, B. Tadić, and N. Gupte, Phys. Rev. E **104**, 034206 (2021).

[59] G. A. Gottwald, Chaos **25**, 053111 (2015).

[60] R. S. Pinto and A. Saa, Phys. Rev. E **92**, 062801 (2015).

[61] https://github.com/SangitaDutta1/Perfect-Synchronization.git.